Soft Nano-Imprint Lithography of Rare-Earth-Doped Light-Emitting Photonic Metasurface

Zeinab Chehadi, Michele Montanari, Nicoletta Granchi, Mehrnaz Modaresialam, Mathieu Koudia, Mathieu Abel, Magali Putero, David Grosso, Francesca Intonti, and Marco Abbarchi*

Sol–gel chemistry and nano-imprint lithography (soft-NIL) can be combined for the fabrication of nano-patterns with large vertical aspect ratio over large scales. The possibility to frame via soft-NIL metal oxides materials featuring a large refractive index and low absorption coefficient, opens new avenues for light management. In spite of its importance, the integration of light emitters in these materials has been mostly investigated in flat layers, limiting their efficiency and versatility. Here it is shown that ZrO_2 can be combined with light emitting Eu^{3+} ions and framed via soft-NIL to form large arrays of pillars atop a 2D residual layer. The chemical precursor solutions and the nano-imprint technique are developed for photonic metasurfaces sustaining sharp resonances ascribed to quasi-guided modes and lattice modes, as accounted for by finite difference time domains simulations. These resonances enable for a record extraction of the Eu^{3+} forward emission up to ≈200 times with respect to the flat counterpart within a relatively small detection angle (≈±16° around the vertical direction). These results are relevant for light-emitting displays, down- and up-conversion processes for light detection such as scintillators for X-ray and for light amplifiers based on rare-earth emitters.

Z. Chehadi, M. Koudia, M. Abel, M. Putero, D. Grosso, M. Abbarchi
IM2NP (UMR 7334)
CNRS
Aix Marseille Univ
Université de Toulon
Marseille F-13397, France
E-mail: marco.abbarchi@im2np.fr
M. Montanari, N. Granchi, F. Intonti
LENS
University of Florence
Sesto Fiorentino 50019, Italy
M. Montanari, N. Granchi, F. Intonti
Department of Physics and Astronomy
University of Florence
Sesto Fiorentino 50019, Italy
M. Modaresialam, D. Grosso, M. Abbarchi
Solnil
95 Rue de la République, Marseille 13002, France

1. Introduction

Photonic metasurfaces are appealing solutions for light manipulation thanks to their compactness and tailorable response to optical excitation emerging from the collective response of the constituent meta-atoms.[1] When metallic or dielectric sub-wavelength particles are arranged in periodic arrays with a pitch close to the wavelength of the incident light, reflection (or transmission) spectra display sharp resonances that are exploitable on a wide range of applications such as sensing[2] surface-enhanced Raman spectroscopy,[3] structural colors,[4] non-linear optics,[5] photovoltaics,[6] meta-optics,[7] and much more.

Integration of light sources within photonic metasurfaces (e.g., quantum dots,[8] impurities,[9] dye molecules,[10,11] and nanocrystalline diamond[12]) and coupling their emission with high quality-factor, collective resonances, extend the use of these devices providing a better control of the photoluminescence emission and improving extraction efficiency and directionality of the radiation in the far-field. However, this task is often hindered by the intrinsic limits of the emitters (e.g., scarce resistance to high temperature annealing during fabrication, lack of room-temperature emission) and complicate fabrication techniques.

Phosphors based on rare earth[13,14] are room-temperature emitters whose luminescence covers a broad spectral range (from ultraviolet to infrared), has a long lifetime (≈ms) and a very large quantum efficiency (almost 100%). Thanks to their processability (e.g., resistance to high temperature annealing), they can be integrated in a solid matrix (e.g., Si,[15] SiN[16]), organic compounds,[17] oxides,[13,18] or framed as nano-particles.[19] They can be exploited in many applications: bio-labels,[20] fiber-laser,[21] displays,[22] solar cells,[23] and X-ray imaging[24] are only few examples. Yet, the forbidden nature of the emitting 4f–4f transitions largely limits their absorption cross-section (≈$10^{-20}cm^2$) and in turn the light emission from these energy levels. Enhancement of the emission was obtained integrating plasmonic particles and rare earths exploiting an energy-transfer mechanism.[25–27] However, at visible and near infrared frequency, metals have a relatively large absorption limiting their applicability.

**ADVANCED
SCIENCE NEWS**

www.advancedsciencenews.com

**ADVANCED
OPTICAL
MATERIALS**

www.advopticalmat.de

Sol–gel chemistry and nano-imprint lithography (soft-NIL) can be combined to obtain, in few simple steps, nano-patterns over large scales[28–32] on arbitrary substrates (e.g., metals, plastic, semiconductors, and glasses). Among the large number of materials that can be molded by soft-NIL, metal oxides are extremely valuable for photonic applications thanks their large refractive index and low absorption coefficient. Following this technique, 3D structures (pillars or holes) atop a 2D layer can be created in a single step.[31,32] It has been recently demonstrated that this residual layer acts as a waveguide.[28] Sharp resonances featuring large-Q factors, in reflection and transmission spring from the coupling of lattice modes of the pillars array and the guided modes in the 2D layer. So far, the integration of light emitters via soft-NIL or similar methods has been limited and the enhancement of light extraction from rare earth emission did not exceed ten times with respect to the flat counterpart.[33–35]

Here we exploit sol–gel chemistry and NIL to integrate rare earth emitters in photonic metasurfaces in a single and simple fabrication step. We combine ZrO_2 with Eu^{3+} ions and print large arrays of cylindrical pillars arranged in a square lattice. Detailed structural and spectroscopic characterizations account for the high quality of our samples, supported by the comparison with finite-difference time-domain (FDTD) simulations: we experimentally observe the formation of sharp resonances typical of a square lattice ascribed to quasi-guided modes.[28] The coupling between these resonances and the photoluminescence of Eu^{3+} leads to a ≈200 times enhancement of emission with respect to the flat counterpart within a relatively small angle (≈±16° around the vertical direction).
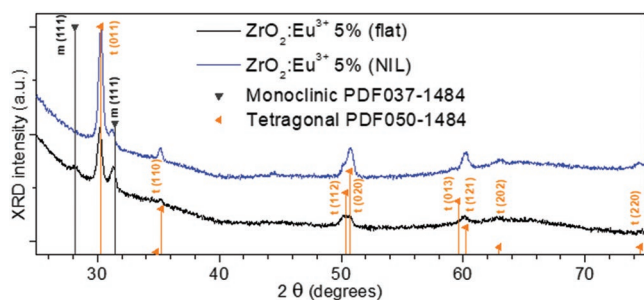
2. Results

2.1. Structural Characterization of the Photonic Metasurfaces

A detailed description of the sample fabrication is provided in the dedicated Section 4. The ZrO_2:Eu^{3+} layers are printed via soft-NIL in 25 arrays each of them having a lateral extension of 2 mm × 2 mm, on fused silica slides (**Figure 1**a). From an optical inspection the arrays feature a high homogeneity (as also accounted for by Fourier transform of the real-space microscope images, Figure 1b) and are almost defect-free; most of the defects occur from extrinsic impurities introduced during sample preparation.

Scanning electron microscopy (SEM) images of the fabricated structures (Figure 1c–e) for a pattern having the smallest pitch (1A, a = 370 nm, other examples are shown in Figure S1, Supporting Information) show that the ZrO_2:Eu^{3+} pillars are organized in a regular square array. From a tilted view (at 52° SEM incidence) they reveal a cylindrical shape with vertical walls and a slightly rounded top (Figure 1c,d). It is also possible to detect the presence of small grains (less than 50 nm in size) composing the pillars and the 2D residual layer underneath (more details will be provided later via X-ray diffraction [XRD]). In order to assess the possible impact of these grains on light scattering, by spectrophotometry, we measured the diffusion from flat layers from near-UV to near-infrared (see Figure S2, Supporting Information). This analysis shows that overall, the scattering generated by the sol–gel coatings is very similar to that of the underlying fused silica wafer (about 1%) used for soft-NIL, accounting for the optical-grade quality of our method. This low scattering does not perturb the light
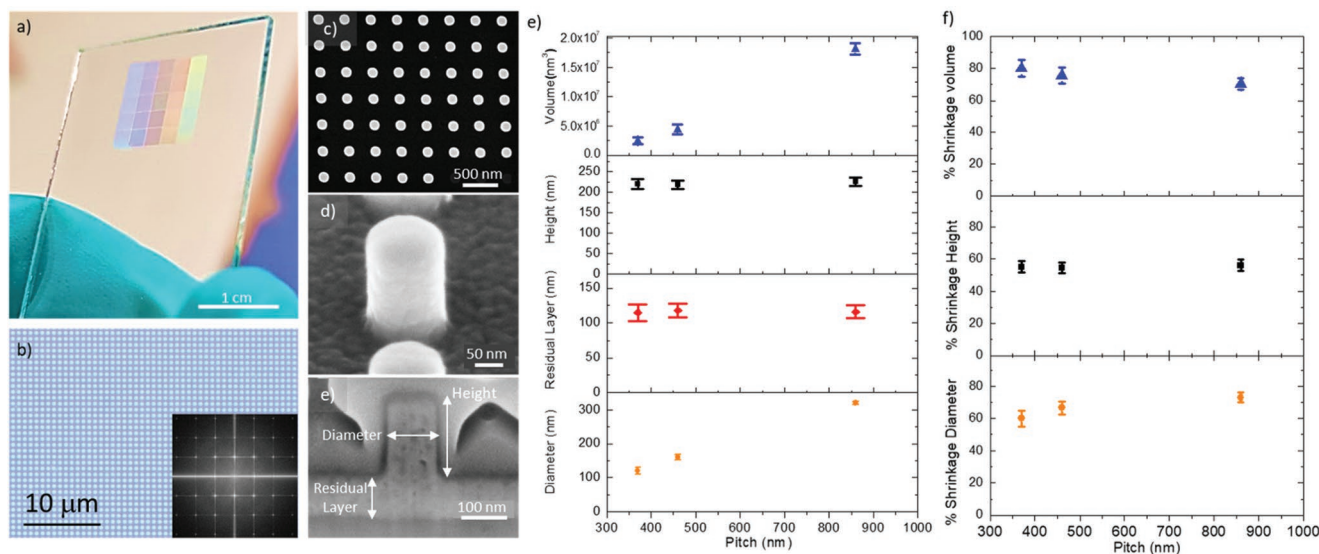
Figure 1. Structural characterization. a) Picture of a ZrO_2:Eu^{3+} layer with 25 arrays covering a 1 cm² area, printed via soft-NIL. b) Optical microscope dark-field image (100× magnification) of array 5E (pitch a = 860 nm). The inset shows a Fourier transform of a larger microscope image. c) Scanning electron micrographs (SEM) at normal incidence of array 1A having a pitch a = 370 nm. d) SEM of an individual pillar at 52° tilted view from array 1A. e) SEM of a section of a pillar at 52° tilted view from array 1A. The pillar diameter, height, and underlying residual layer are highlighted. Additional SEM images are provided in Figure S1, Supporting Information. f) From the bottom to the top panel, respectively: pillar diameter, residual layer thickness, pillar height, and volume as a function of the corresponding pitch a for the cases 1A (a = 370 nm), 1E (a = 470 nm), and 5E (a = 860 nm). g) Shrinking of the printed ZrO_2 structures with respect to the original Si master. From the bottom to the top panel, respectively: diameter, height, and volume shrinking.

**ADVANCED
SCIENCE NEWS**

www.advancedsciencenews.com

**ADVANCED
OPTICAL
MATERIALS**

www.advopticalmat.de

Figure 2. X-ray diffraction spectra (XRD) of flat layer (flat) and textured surface (NIL). The m and t are labels to monoclinic and tetragonal phases.

propagation in the flat layer and is a key feature for high-quality photonic devices.

By cutting the structures with a focused ion beam, we measure the height of the pillars and the thickness of the residual layer (Figure 1e). Overall, we can reconstruct the main structural features of the printed structures that, for three investigated cases, are summarized as follows (Figure 1e): when changing the pitch a from 370 to 860 nm the corresponding diameter increases linearly from 100 to 270 nm; the residual layer and the pillars height are constant and are respectively 130 ± 10 and 193 ± 10 nm; the pillars volume increases linearly from 0.25 ± 0.05 to $1.54 \pm 0.09 \times 10^7$ nm^3.

Considering the initial size of the pillars on the Si master used for soft-NIL, we can estimate the shrinking of pillars diameter, height, and volume. These values are rather constant for the three investigated cases and are about 60%, 55%, and 75% (respectively, Figure 1f) bottom, central, and top panels). This analysis reveals a relevant shrinkage of sol–gel material owing to evaporation of the solvent upon high-temperature annealing and calcination. This feature is extremely important and must be taken into account when designing the Si master targeting a certain final design (e.g. a filling fraction of the metal oxide pillars).

2.1.1. X-Ray Diffraction and Photoelectron Spectroscopy

XRD was performed to check the crystalline phases of flat and nanoimprinted films (**Figure 2**). Both imprinted and flat, sol–gel layers feature a crystalline structure composed of monoclinic (Mono.) and tetragonal (Tetra.) phases, as expected for ZrO$_2$ combined with a few percent of a rare earth cation in substitution.[36] No cubic phase was found. From Rietveld refinement, we deduce that Mono. and Tetra. phases in both samples

have larger lattice volumes (peaks are clearly shifted to smaller angles) compared to pure ZrO$_2$ phases, due to the larger size of europium (III) cation (**Table 1**).

Differences can be observed between the plain and the imprinted samples, suggesting that the nano-imprint step influences the distribution of the rare earth cation in both phases. The plain coating has smaller tetragonal grains in less quantity. The imprinted coating shows larger tetragonal grains in larger amount (81%) and smaller monoclinic grains.

This larger grain-size contrast is likely related to the higher degree of freedom available to the tetragonal phase to grow from the monoclinic one in the imprinted sample rather than in the 2D plain layer. In both cases, the monoclinic grains feature a larger lattice increase, whereas the (111) texture of the monoclinic grains is more pronounced in the imprinted material.

Further insight in the composition and organization of the ZrO$_2$:Eu^{3+} crystal can be inferred by X-ray photoelectron spectroscopy (XPS, see the Figure S4, Supporting Information). These measurements were performed on a thin film deposited atop a low-resistivity, Si bulk wafer. We identified two peaks at 185.09 and 182.68 eV corresponding to Zr3d$_{3/2}$ and Zr3d$_{5/2}$.[37] The emission at 530.52 eV corresponds to O1$_s$ from ZrO$_2$ while 532.1 and 533.19 eV correspond to oxygen in adsorbed water as already described in the literature.[38] Peaks at 1164.58 and 1134.89 eV are assigned to Eu3d$_{3/2}$ and Eu3d$_{5/2}$ in a (III) oxidation state, whereas the weak ones at 1156.41 and 1127.06 eV reveal a few amount of Eu3d$_{3/2}$ and Eu3d$_{5/2}$ in a (II) oxidation state.

2.2. Optical Spectroscopy

2.2.1. Light Reflection

A collimated beam of white light is shined on the printed structures through an objective lens (NA = 0.28) allowing to illuminate all the wavevectors between ±16° with respect to the sample normal. Angular and spectral dependence of light reflection is detected by Fourier-space imaging (**Figure 3**a, top panel): the image of the back focal plane (Fourier plane) of the objective lens is formed on the entrance slit of the spectrometer by means of a secondary lens (not represented), assigning an angle θ (measured with respect to the normal to the sample surface) to a point at a defined distance R from the optical axis.

The dispersion of the spectral features of the square lattices can be detected along the main directions of the first Brillouin zone (e.g., from Γ toward M or toward X; Figure 3a, bottom panel) by aligning these directions (e.g., rotating the sample) with

Table 1. Summary of X-ray diffraction (XRD) measurements. Plain and imprinted samples are respectively 2D layers and textured layers via soft-NIL. From the analysis of the XRD spectra (Figure 2) two crystalline phases are identified, monoclinic (Mono.) and tetragonal (Tetra.). We extracted lattice changes, grain size, and the texture.

Sample	Phase	Compos. vol. [%]	Lattice $(V-V_0)/V_0$ [%]	Grain size [nm]	Texture
Plain	Mono.	59	+1.08	18 ± 5	High (111)
	Tetra.	41	+0.71	28 ± 15	
Imprinted	Mono.	19	+1.34	12 ± 5	Very high (111)
	Tetra.	81	+0.23	35 ± 10	
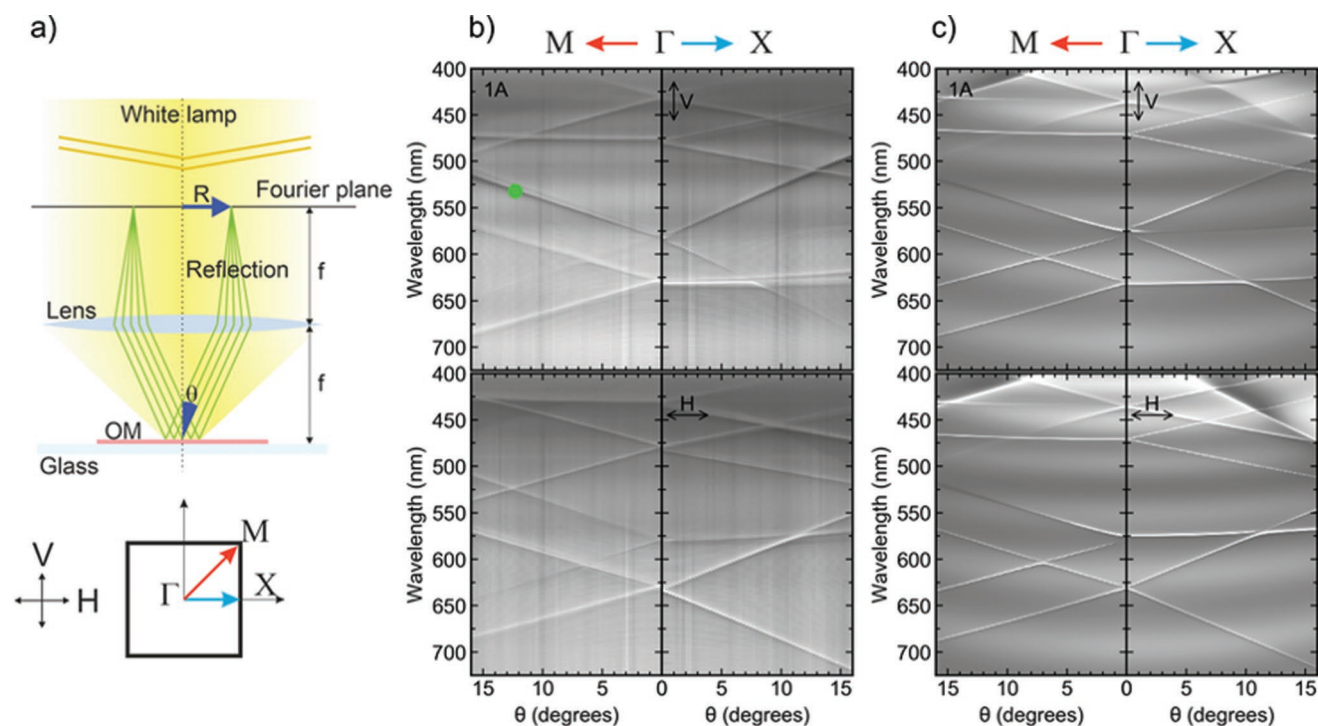
Figure 3. Reflection measurements. a) Top panel: Scheme of the illumination an collection geometry. A beam of white light is collimated and shined on the sample through an objective lens. The light reflected from the sample at specific angles (e.g., green lines) converges in a defined point on the back focal plane of the objective lens (Fourier plane). This plane is imaged through a second lens on the entrance slit of the spectrometer (not shown). Bottom panel: Scheme of the Brillouin zone highlighting the symmetry points and directions as well as the choice of vertical (V) and horizontal (H) polarization directions. b) Angular dependence of the reflected light for the array 1A (a = 370 nm). The top (bottom) panel displays the vertical (horizontal) polarization. For each panel, the left (right) part displays the dispersion along the Γ-M (Γ-X) direction. The experimental data are normalized to the spectrum of the white light used for illumination. c) Finite-difference time-domain (FDTD) of the same structure measured in (b).

the spectrometer entrance slit that is kept open at about 50 μm. The reflected light is discriminated using a linear polarizer.

Several sharp resonances with different slope are observed in reflection measurements for vertical V and horizontal H polarization, respectively parallel and orthogonal with respect to the spectrometer entrance slit (Figure 3b). The dispersion of these resonances are typical of a square photonic lattice and are well reproduced by FDTD simulations taking into account the structural information of pitch a, pillar height, and diameter, residual layer thickness and material refractive index (Figure 3c).
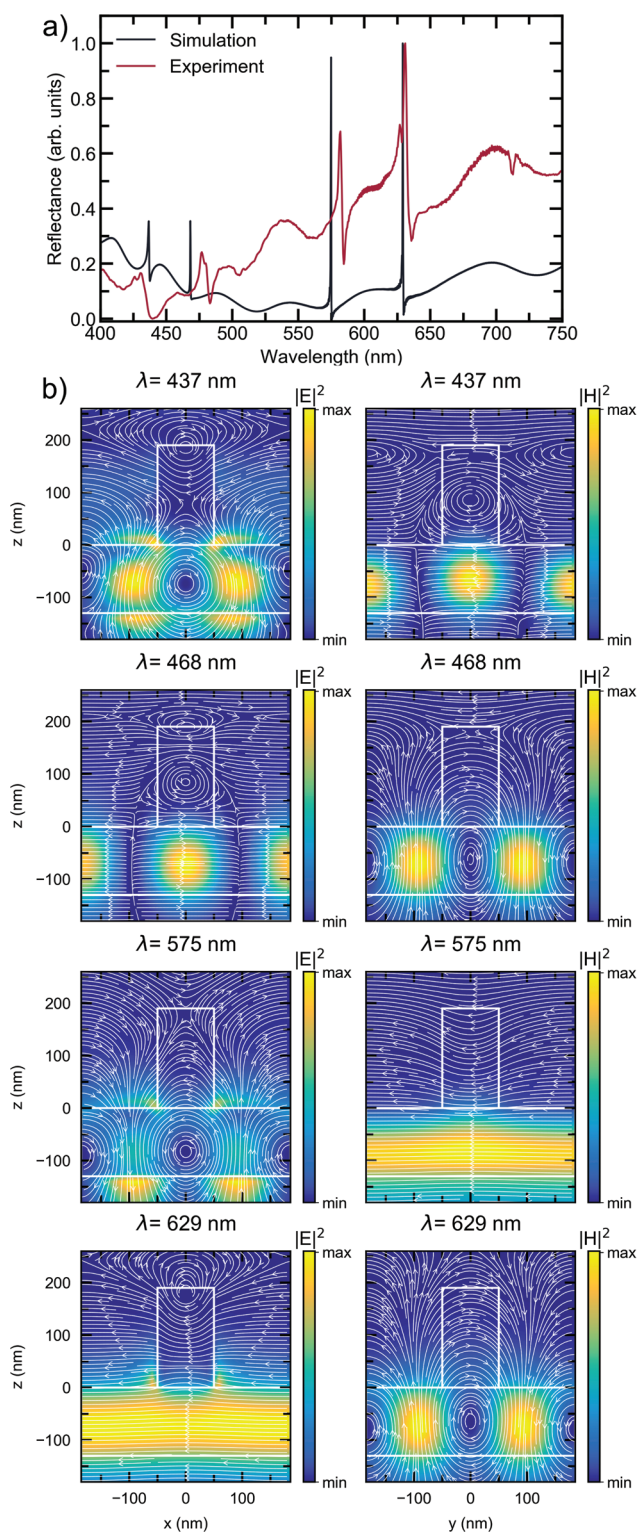
A deeper insight in the features and nature of the detected resonances is obtained by FDTD simulations of the crosscuts of the electromagnetic field current loops inside the structures. The experimental and simulated spectra at the Γ-point band edge, that is, vertical cuts at $\theta = 0°$ in Figure 3b,c, are reported in **Figure 4**a). Small deviations between experiment and simulations at shorter wavelength can be related to imperfections in the fabricated structures, to the fact that in numerical calculations we assumed a constant refractive index (n = 2.05) and to the simplification of the actual shape of the pillars (rounded top not considered).

The spectra show four narrow peaks in pairs, respectively at 437/468 and 575/629 nm (Figure 4a). The simulation of magnetic and electric field distributions in the cross-cut at 629 nm (Figure 4b) shows that they are both strongly confined in the

2D residual layer underneath the 3D pillars and, from the circulation of the magnetic field intensity H^2, we conclude that there is an electric guided mode in the layer propagating along the y-axis.[28] Thus, we refer to this mode as E-QGM1. Following the same argument we can refer to the modes at 575, 468, and 437 nm as M-QGM1, E-QGM2, and M-QGM2, respectively. Quasi-guided modes require a waveguide with a refractive index higher than the surrounding medium to be observed and, indeed, the sharp peaks of Figure 4a) are not observed in simulations where the pillars are directly atop the silica substrate (not shown).

2.2.2. Photoluminescence Emission

Room temperature photoluminescence above 550 nm from 2D flat layers deposited atop fused silica wafers reveals a complex structure of energy levels corresponding to the transitions 5D0 to 7F1-7F5, which are characteristic of the f–f transition of Eu^{3+} ions[13,14,17] (see Figure S3, Supporting Information). These transitions are more evident (more intense and sharp) when the sol–gel layer is annealed at the maximal temperature of 1200 °C for 10 min. Thus, we select these annealing conditions to process the printed structures (similar results to those shown here were also observed in a printed sample annealed at 800 °C for 10 min, not shown).

ADVANCED
SCIENCE NEWS
www.advancedsciencenews.com

ADVANCED
OPTICAL
MATERIALS
www.advopticalmat.de

Figure 4. a) Comparison between the measured reflection spectrum (red curve) and the spectrum simulated by FDTD calculations (black curve). b) Electric (left column) and magnetic (right column) field intensity distributions and current loops (white arrows). The maps, acquired at the wavelength of the peaks of the black curve in panel (a), are reported in order of increasing wavelength from top to bottom. The shape of the nanopillar and the boundaries of the residual layer are indicated with the white lines.

Photoluminescence from the printed structures is detected, as for light reflection, by Fourier space imaging (**Figure 5**a). In this case, the laser is shined at about 12° of incidence with respect to the normal to the sample surface (green dot in Figure 3b), where a resonance is available for coupling the light in the structure). Different excitation angles are chosen for structures with different pitch (not shown).

For the smallest pitch (pattern 1A, $a = 370$ nm) an intense emission is observed in the far-field (Figure 5b). When discriminating the polarization and observing the dispersion from Γ to X we can see that the photoluminescence couples to the fast and slow modes with a large enhancement in about ±5° with respect to the sample normal.
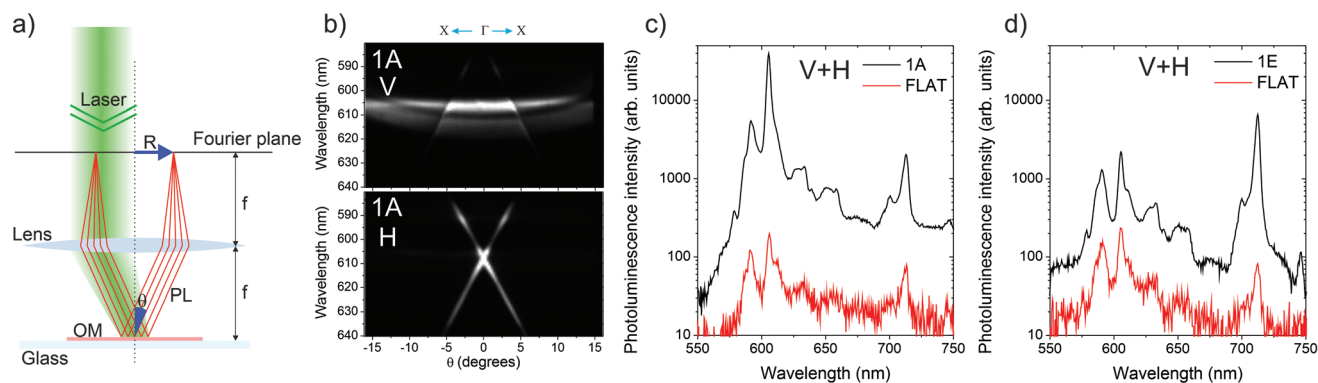
Integrating this emission over the accessible solid angle (within the NA of the objective lens), and comparing with the emission of the flat layer, we observe a large enhancement (up to about 200 times) at 605 nm for the pattern 1A ($a = 370$ nm) and about 80 times at about 712 nm for the array 1E ($a = 460$ nm).

Although other metal oxides may be more suitable crystalline hosts for Eu^{3+} emitters (e.g., Y_2O_3 thanks to its intrinsic features of charge and radius), the photoluminescence intensity extracted from our ZrO_2 structures is bright enough to be visible by naked eyes and can be easily detected with a smart-phone camera, either directly imaging the sample, or by observing it diffused on a white paper sheet placed at about 1 m from the sample surface (see Figure S4, Supporting Information). At this distance the photoluminescence beam can be as small as a few mm, accounting for its small angular spread and feature a square section, reflecting the dispersion of the underlying photonic resonances.

As an alternative way to use our devices, we also measured the photoluminescence emission from the back side of the sample (inset of **Figure 6**). In this case, we did not use any lens to collect the light, but just a fiber boundle (910 μm core, placed at about 1 mm from the back surface of the sample. Comparing the emission with respect to the flat part, we observe again a large enhancement of about 25 times without any optimization.

2.3. Discussion

Our soft-NIL fabrication method for photonic metasurfaces working at visible and near-infrared frequency has several advantages with respect to conventional approaches. Standard nano-fabrication methods in fact, typically involve rather complex processes. Deep-UV optical lithography and e-beam lithography are well established paradigms in this field that require several steps: 1) deposition of a 2D, thin layer (e.g., via chemical vapor deposition, sputtering, pulsed laser deposition); 2) deposition of a photoresist atop (e.g., via spin-coating); 3) patterning of the photoresist via UV light illumination (e.g., through a mask) or via an electron beam; 4) chemical development of the exposed areas; 5) chemical cleaning of these parts; 6) top-down etching to physically remove the exposed parts of the hard material (e.g., reactive ion etching, inductively coupled plasma, chemical etching); and 7) chemical cleaning of the remaining photoresist. These steps render conventional

2201618 (5 of 9)

**ADVANCED
SCIENCE NEWS**

www.advancedsciencenews.com

**ADVANCED
OPTICAL
MATERIALS**

www.advopticalmat.de

Figure 5. Photoluminescence spectroscopy: front emission. a) Scheme of the excitation and collection configuration. A green laser at 532 nm is shined on the sample surface at tilted incidence. The emitted photoluminescence coupled to the photonic modes is directed to specific directions forming an image on the back focal plane of the objective lens (the Fourier plane). The image of this plane is formed with a second lens on the entrance slit of the spectrometer (not shown). b) Top and bottom panels display, respectively, the angle-resolved emission from pattern 1A (a = 370 nm) for vertical (V) and horizontal (H) polarization. c) Angle- and polarization-integrated photoluminescence emission from pattern 1A (black line) compared to the 2D flat layer (red line). d) Same as (c) for pattern 1E (a = 440 nm).

deep-UV photolithography and e-beam lithography time-consuming and expensive.

NIL is an industrial method conventionally used for polymers. For metal oxides, soft-NIL allows to exploit sol–gel chemistry (e.g., conceiving many different formulations[39]) and directly shape 3D structures on large substrates (up to 10 cm wafers[40]) eventually featuring a large dielectric constant[29,31,32]. Hybrid materials, tunable porosity, and large aspect ratio of the printed structures are a few examples of its versatility.[40] It requires a reduced number of simple fabrication steps: 1) spin coating of the sol–gel solution; 2) mold application (that in our case does not require pressure; 3) consolidation; 4) demolding; and 5) calcination at high temperature. It can be realized in less than 20 min in a research laboratory (depending on the calcination step) and is compatible with commercial, automatic machines working on 20 cm wafers.

Integration of light emitters at visible and near-infrared frequency has been implemented in photonic metasurfaces exploiting several strategies:[41–43] colloidal quantum dots,[44] organic molecules,[45] or 2D materials[46–48] are only few examples of possible solutions. However, in all these cases the emitters are not directly integrated within the dielectric structures. Ge-based quantum dots grown by epitaxy are a viable alternative to embed light emitters within silicon-based photonic devices[49,50]. Yet, this latter approach is costly and hardly scalable.

In the context of photonic metasurfaces based on dielectric materials, integration of rare earths was first achieved in thin films of Al_2O_3 and Y_2O_3 further functionalized by soft-NIL[33] or reverse NIL,[34,35] providing enhancements of the emission below ten times with respect to the flat counterparts. More recently, Eu^{3+} ions embedded in Y_2O_3 thin films[51] were topped by a Si_3N_4 layer post-processed by lithography, showing a record of light absorption and extraction exploiting a doubly resonant metasurface: near-UV excitation at normal incidence and extraction at about 60° resulted in a global emission enhancement of about two order of magnitude with respect to the flat counterpart.

Concerning the performances of our devices in extracting light with respect to those obtained with similar fabrication approaches based on NIL[33–35] we observe an improvement of at least one order of magnitude. A possible reason for this improved extraction could be ascribed to the presence of relatively low grains (20–30 nm, Table 1) limiting the Rayleigh scattering and thus propagation losses in the slab.

Comparing to more performing devices, such as those shown in ref. [51] obtained via conventional lithography, we observe that in our case we only optimize the extraction efficiency whereas absorption is not taken into account. We infer that
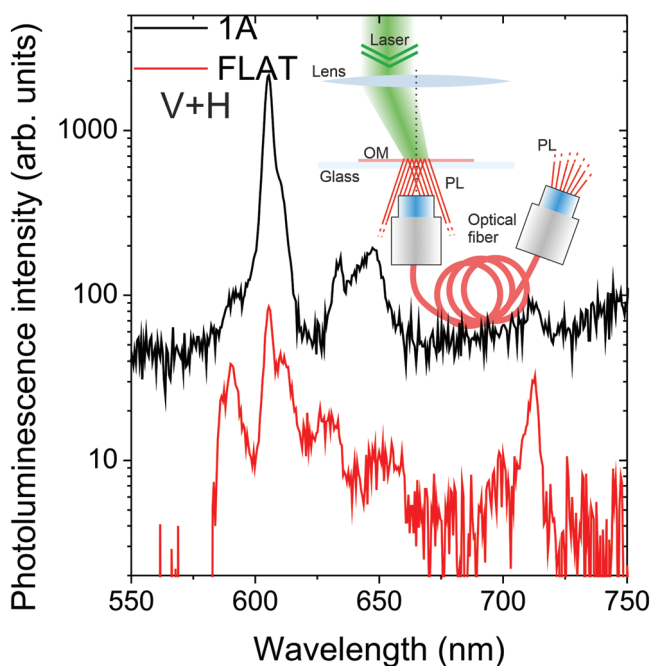
Figure 6. Photoluminescence spectroscopy: back emission. Photoluminescence intensity from pattern 1A (a = 370 nm) collected with a fiber boundle placed at less than 1 mm from the back of the photonic metasurface, that is excited from the front part (as shown in the inset of the figure). The emission from the flat part is shown as a reference.

further increase in the emission could be in principle obtained with an optimized design of the Si-master. Furthermore, our choice allows an extraction at normal incidence within a relatively small angle, that is more convenient for applications in displays or light detectors with respect to a tilted emission.

3. Conclusion

In conclusion, we showed that soft-NIL, a direct nano-fabrication method compatible with industrial processing, can be efficiently exploited for the fabrication of light emitting, photonic metasurfaces integrating rare earths. Our formulations of the sol–gel material and thermal processing allows to largely improve the light extraction with respect to similar devices: we can channel in a low numerical aperture, objective lens up to 200 times more light with respect to the flat counterpart, accounting for a highly directional emission. These results can be extended to other rare earth emitters such as Er^{3+}, Ce^{3+}, and others as well as other metal oxides, such a TiO_2 and SiO_2.

Our results are important in view of the exploitation of soft-NIL for active, photonic metasurfaces for displays, devices for telecommunication, down-conversion layers for applications in photovoltaic and light-detectors.

4. Experimental Section

Silicon Master: The silicon master was elaborated by electron beam lithography and reactive ion etching on a bulk silicon wafer. It contained 25 arrays of cylindrical pillars with a height of 400 nm organized in a square geometry. Each array had an overall size of 4 mm². The pillar diameter D increased from 200 to 460 nm in steps of 10 nm. The pitch a was chosen as the double of the diameter: $a = 2D$. This choice fixed the filling fraction of the pillar within the unit cell as constant through the 25 arrays.

Mold Preparation: The mold was prepared by the following procedure: i) the surface of the Si master was functionalized with silane group by using 1H,1H,2H,2H-perfluorooctyltri ethoxysilane in vapor phase for about 12 h to decrease the surface energy and reduce the interactions with the PDMS chains; ii) a bi-layer hard-PDMS/PDMS was then deposited in two steps: 1) by spin-coating a thin layer of hard-PDMS onto the functionalized master surface and 2) by pouring a mixture of PDMS precursors reactants (90 wt% RTV141A; 10 wt% RTV141B from BLUESIL) on top of the hard PDMS; iii) the bi-layer hard-PDMS/PDMS stamp was cured at 70 °C for about 12 h before demolding.

Nanoimprint Lithography Process: With modifications in the procedure's steps, the samples were fabricated in this work according to the following process: vapor pressure thermal NIL. This process was elaborated before in the team by Bottein et al.[39] Particularly, ZrO_2 sol–gel combining with Eu^{3+} was used for the first time to imprint large area of cylindrical pillars. For the fabrication of ZrO_2-Eu^{3+} replicas, the precursor solution was prepared following these steps: i) mixing 1 $ZrCl_4$:30 EtOH: 5 H_2O: 5×10^{-4} F127 (Pluronic F127: polyethylene oxide-polypropylene oxide triblock copolymer, PEO-PPO-PEO, from Aldrich): 9×10^{-3} CTAB ($[(C_{16}H_{33})N(CH_3)_3]Br$; hexadecyltrimethyl ammonium bromide) molar ratios; ii) after 24 h of aging, 5% of $EuCl_3 \cdot 6H_2O$ was added to the solution; in order to integrate the light source in sol–gel solution, this step was added in the process of preparing the precursor solution used in this work; iii) after 2 h of aging, the solutions were dip-coated on fused silica substrates at a constant withdrawal rate 2 mm s⁻¹ under controlled relative humidity (RH = 10%); iv) after the dip-coating process, the films were exposed to a water-vapor treatment for 10–20 s; the water vapor treatment step

was added in this work which promoted the diffusion of water within the coating film and allowed the reorganization of ZrO_2:Eu^{3+} film into a highly ordered mesophase;[30] iv) the PDMS mold was pumped for 10 min under primary vacuum and then readily applied (in less than 1 min after dip coating) on the as-deposited sol–gel thin film into a nanoimprint chamber with temperature and relative humidity control.[39] The relative humidity was maintained in the soft-NIL chamber at 50% for ZrO_2-Eu^{3+} xerogel film; v) before unmolding, the system was cured at 70 °C for 20 min; and vi) the imprinted samples were then annealed at high temperature (500–1200 °C) for 10 min by using tubular oven in order to investigate the influence of temperature annealing on the photoluminescence of Europium and crystalline phase of zirconium.

X-Ray Diffraction Measurements: XRD patterns were recorded on a conventional diffractometer (PANalytical Empyrean) using Cu radiation ($\lambda = 0.154$ nm) and a rapid detector (PANalytical PIXcel) in Bragg–Brentano geometry. From X-ray powder diffraction data both monoclinic (space group P21/c) and tetragonal (space group P42/nmc) structure of ZrO_2 phase were refined using a Rietveld-type method[52] and the Profex software to deduce the percentage of each phase, average grain size, and cell parameters.

X-Ray Photoelectron Spectroscopy: XPS experiments were performed in a ultra-high vacuum chamber at 10^{-10} mbar with a monochromatized Al Kα X-ray radiation (1486.7 eV) of an Omicron XM1000 source. Spectra were recorded at 20° emission angle with an Omicron EA125 analyzer and a 10 eV pass energy. Voigt functions (Gaussian–Lorentzian 70%/30%) components were used for the deconvolution of the XPS spectra after subtraction of a Shirley background. C1s peak at 284.8 eV had been taken as a reference position peak to estimate the energy of the other peaks.

Optical Spectroscopy: Refractive index, thickness, and porosity of flat sol–gel layers were assessed via ellipsometry (Wollam M200V ellipsometer, 350–1000 nm) and ellipsometry porosimetry (see Figure S2, Supporting Information).

Optical spectroscopy on flat sol–gel layers was performed by using a spectrophotometer (from PerkinElmer) mounting an integrating sphere measuring total reflection, total transmission, and reflected diffusion (see Figure S2, Supporting Information).

Fourier-spectroscopy on the printed structures was performed using a custom-made confocal setup. For light reflection measurements a white halogen lamp (from Oriel Instrument) was used whereas photoluminescence was excited by a solid-state laser source emitting at 532 nm. The light sources were shined on the sample using a 10× objective lens having a numerical aperture of 0.28 (from Mitutoyo). An image of the back focal plane of the objective was formed on the entrance slit of a 30 cm spectrometer (from Andor) and dispersed with a 150 gpmm grating. The light was detected with a Si-based CCD-Camera (Newton, from Andor).

Finite-Difference Time-Domain Simulations: The electromagnetic simulations were performed using the commercial FDTD software Lumerical.[53] The ZrO_2 pillar refractive index was set to 2.05 and the geometrical parameters were those obtained by the structural characterization, the residual layer had a refractive index of 2.05 and thickness 130 nm, while the refractive index of the semi-infinite fused silica substrate was set to $n = 1.46$. The metasurface was illuminated by a broad band ($\lambda = 350-750$ nm) plane wave from the top. Power transmission monitors were positioned above the source to obtain the reflectance, and two field monitors intersect the pillar along the xz and yz plane to monitor the local field intensity. One period of the metasurface was simulated by using periodic boundary condition in x and y-normal plane, whereas perfectly matched layer boundary conditions were used in the z-normal plane.

Supporting Information

Supporting Information is available from the Wiley Online Library or from the author.

Conflict of Interest

The authors declare no conflict of interest.

Data Availability Statement

The data that support the findings of this study are available from the corresponding author upon reasonable request.

[1] J. Hu, S. Bandyopadhyay, Y.-h. Liu, L.-y. Shao, *Front. Phys.* **2021**, *8*, 586087.

[2] Y. Lee, S.-J. Kim, H. Park, B. Lee, *Sensors* **2017**, *17*, 1726.

[3] S. Gwo, C.-Y. Wang, H.-Y. Chen, M.-H. Lin, L. Sun, X. Li, W.-L. Chen, Y.-M. Chang, H. Ahn, *ACS Photonics* **2016**, *3*, 1371.

[4] T. Wood, M. Naffouti, J. Berthelot, T. David, J.-B. Claude, L. Métayer, A. Delobbe, L. Favre, A. Ronda, I. Berbezier, N. Bonod, M. Abbarchi, *ACS Photonics* **2017**, *4*, 873.

[5] A. Krasnok, M. Tymchenko, A. Alù, *Mater. Today* **2018**, *21*, 8.

[6] P. Spinelli, M. Verschuuren, A. Polman, *Nat. Commun.* **2012**, *3*, 692.

[7] M. Khorasaninejad, F. Capasso, *Science* **2017**, *358*, eaam8100.

[8] N. Ganesh, W. Zhang, P. C. Mathias, E. Chow, J. A. N. T. Soares, V. Malyarchuk, A. D. Smith, B. T. Cunningham, *Nat. Nanotechnol.* **2007**, *2*, 515.

[9] L. Zhu, S. Yuan, C. Zeng, J. Xia, *Adv. Opt. Mater.* **2020**, *8*, 1901830.

[10] Y.-T. Lin, A. Hassanfiroozi, W.-R. Jiang, M.-Y. Liao, W.-J. Lee, P. C. Wu, *Nanophotonics* **2021**, *11*, 2701.

[11] S. Murai, G. W. Castellanos, T. V. Raziman, A. G. Curto, J. G. Rivas, *Adv. Opt. Mater.* **2020**, *8*, 1902024.

[12] J. Fait, M. Varga, K. Hruska, Z. Remes, V. Jurka, A. Kromka, B. Rezek, L. Ondic, *Nanophotonics* **2019**, *8*, 1041.

[13] K. Binnemans, *Chem. Rev.* **2009**, *109*, 4283.

[14] K. Binnemans, *Coord. Chem. Rev.* **2015**, *295*, 1.

[15] D. Adler, D. Jacobson, D. Eaglesham, M. Marcus, J. Benton, J. Poate, P. Citrin, *Appl. Phys. Lett.* **1992**, *61*, 2181.

[16] Y. Li, N. Hirosaki, R.-J. Xie, T. Takeda, M. Mitomo, *J. Lumin.* **2010**, *130*, 1147.

[17] T. Oyamada, Y. Kawamura, T. Koyama, H. Sasabe, C. Adachi, *Adv. Mater.* **2004**, *16*, 1082.

[18] E. N. Cerón, G. R. Gattorno, J. Guzmán-Mendoza, M. García-Hipólito, C. Falcony, *Open J. Synth. Theory Appl.* **2013**, *2*, 73.

[19] C. Bouzigues, T. Gacoin, A. Alexandrou, *ACS Nano* **2011**, *5*, 8488.

[20] C. Liu, Y. Hou, M. Gao, *Adv. Mater.* **2014**, *26*, 6922.

[21] M. K. Hossain, S. Hossain, M. H. Ahmed, M. I. Khan, N. Haque, G. A. Raihan, *ACS Appl. Electron. Mater.* **2021**, *3*, 3715.

[22] E. Downing, L. Hesselink, J. Ralston, R. Macfarlane, *Science* **1996**, *273*, 1185.

[23] J. C. Goldschmidt, S. Fischer, *Adv. Opt. Mater.* **2015**, *3*, 510.

[24] A. Pereira, T. Martin, M. Levinta, C. Dujardin, *J. Mater. Chem. C* **2015**, *3*, 4954.

[25] M. Eichelbaum, K. Rademann, *Adv. Funct. Mater.* **2009**, *19*, 2045.

[26] S. Fischer, F. Hallermann, T. Eichelkraut, G. von Plessen, K. W. Krämer, D. Biner, H. Steinkemper, M. Hermle, J. C. Goldschmidt, *Opt. Express* **2012**, *20*, 271.

[27] M. Saboktakin, X. Ye, U. K. Chettiar, N. Engheta, C. B. Murray, C. R. Kagan, *ACS Nano* **2013**, *7*, 7186.

[28] J. A. Garcia, C. Hrelescu, X. Zhang, D. Grosso, M. Abbarchi, A. L. Bradley, *ACS Appl. Mater. Interfaces* **2021**, *13*, 47860.

[29] M. Bochet-Modaresialam, J.-B. Claude, D. Grosso, M. Abbarchi, *ACS Appl. Nano Mater.* **2020**, *3*, 5231.

[30] W. Zhang, J. Tu, W. Long, W. Lai, Y. Sheng, T. Guo, *Energy Procedia* **2017**, *130*, 72.

[31] S. Checcucci, T. Bottein, M. Gurioli, L. Favre, D. Grosso, M. Abbarchi, *Adv. Opt. Mater.* **2019**, *7*, 1801406.

[32] T. Bottein, T. Wood, T. David, J. B. Claude, L. Favre, I. Berbézier, A. Ronda, M. Abbarchi, D. Grosso, *Adv. Funct. Mater.* **2017**, *27*, 1604924.

[33] A. Revaux, G. Dantelle, D. Decanini, F. Guillemot, A.-M. Haghiri-Gosnet, C. Weisbuch, J.-P. Boilot, T. Gacoin, H. Benisty, *Nanotechnology* **2011**, *22*, 365701.

[34] K.-K. Kim, K.-Y. Ko, J. Ahn, *J. Nanosci. Nanotechnol.* **2013**, *13*, 7184.

[35] C. Park, H. Kim, I.-S. Park, K.-Y. Ko, K.-K. Kim, B. H. Lee, J. Ahn, *Microelectron. Eng.* **2015**, *136*, 48.

[36] A. Speghini, M. Bettinelli, P. Riello, S. Bucella, A. Benedetti, *J. Mater. Res.* **2005**, *20*, 2780.

[37] G. Cabello, L. Lillo, C. Caro, G. E. Buono-Core, B. Chornik, M. Soto, *J. Non-Cryst. Solids* **2008**, *354*, 3919.

[38] Y. Gao, Y. Masuda, H. Ohta, K. Koumoto, *Chem. Mater.* **2004**, *16*, 2615.

[39] T. Bottein, O. Dalstein, M. Putero, A. Cattoni, M. Faustini, M. Abbarchi, D. Grosso, *Nanoscale* **2018**, *10*, 1420.

[40] M. Modaresialam, Z. Chehadi, T. Bottein, M. Abbarchi, D. Grosso, *Chem. Mater.* **2021**, *33*, 5464.

[41] Y. Liu, K. Koga, S. Khumpuang, M. Nagao, T. Matsukawa, S. Hara, *Jpn. J. Appl. Phys.* **2017**, *56*, 06GG01.

[42] A. Vaskin, R. Kolkowski, A. F. Koenderink, I. Staude, *Nanophotonics* **2019**, *8*, 1151.

[43] S. Bidault, M. Mivelle, N. Bonod, *J. Appl. Phys.* **2019**, *126*, 094104.

[44] I. Staude, V. V. Khardikov, N. T. Fofang, S. Liu, M. Decker, D. N. Neshev, T. S. Luk, I. Brener, Y. S. Kivshar, *ACS Photonics* **2015**, *2*, 172.

[45] F. Todisco, R. Malureanu, C. Wolff, P. Gonçalves, A. S. Roberts, N. A. Mortensen, C. Tserkezis, *Nanophotonics* **2020**, *9*, 803.

[46] S. Lepeshov, M. Wang, A. Krasnok, O. Kotov, T. Zhang, H. Liu, T. Jiang, B. Korgel, M. Terrones, Y. Zheng, A. Alú, *ACS Appl. Mater. Interfaces* **2018**, *10*, 16690.

[47] A. F. Cihan, A. G. Curto, S. Raza, P. G. Kik, M. L. Brongersma, *Nat. Photonics* **2018**, *12*, 284.

[48] T. Bucher, A. Vaskin, R. Mupparapu, F. J. Lochner, A. George, K. E. Chong, S. Fasold, C. Neumann, D.-Y. Choi, F. Eilenberger,

**ADVANCED
SCIENCE NEWS**

www.advancedsciencenews.com

**ADVANCED
OPTICAL
MATERIALS**

www.advopticalmat.de

F. Setzpfandt, Y. S. Kivshar, T. Pertsch, A. Turchanin, I. Staude, *ACS Photonics* **2019**, *6*, 1002.

[49] V. Rutckaia, F. Heyroth, A. Novikov, M. Shaleev, M. Petrov, J. Schilling, *Nano Lett.* **2017**, *17*, 6886.

[50] S. Yuan, X. Qiu, C. Cui, L. Zhu, Y. Wang, Y. Li, J. Song, Q. Huang, J. Xia, *ACS Nano* **2017**, *11*, 10704.

[51] N.-V. Hoang, A. Pereira, H. S. Nguyen, E. Drouard, B. Moine, T. Deschamps, R. Orobtchouk, A. Pillonnet, C. Seassal, *ACS Photonics* **2017**, *4*, 1705.

[52] N. Doebelin, R. Kleeberg, *J. Appl. Crystallogr.* **2015**, *48*, 1573.

[53] Lumerical inc., Nanophotonic FDTD Simulation Software, https://www.lumerical.com/products/fdtd.

2201618 (9 of 9)